

Differentiable Factor Graph Optimization for Learning Smoothers

Brent Yi¹, Michelle A. Lee¹, Alina Kloss², Roberto Martín-Martín¹, and Jeannette Bohg¹

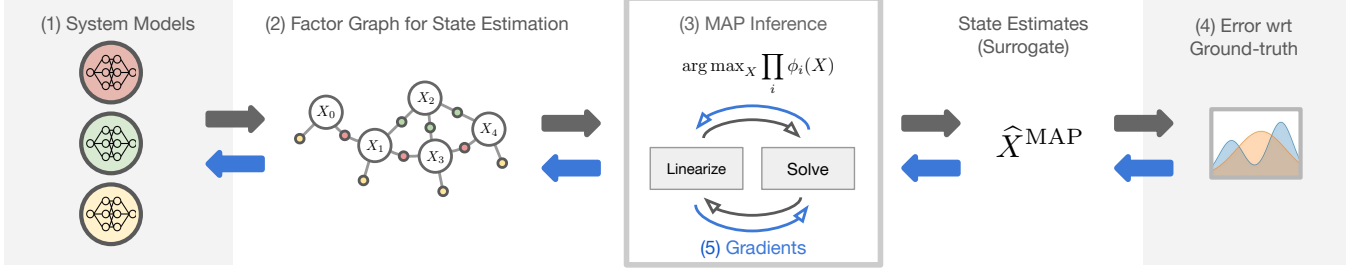


Fig. 1: An overview of our approach for end-to-end learning of factor graph-based smoothers. We (1) start with probabilistic system models, which may be learned or analytical, (2) use them to model state estimation problems as factor graphs, (3) generate a surrogate for posterior estimates by running several steps of a nonlinear optimizer, (4) compute an error with respect to a known ground-truth, and (5) backpropagate estimation errors through the unrolled nonlinear optimizer directly to system model parameters.

Abstract—A recent line of work has shown that end-to-end optimization of Bayesian filters can be used to learn state estimators for systems whose underlying models are difficult to hand-design or tune, while retaining the core advantages of probabilistic state estimation. As an alternative approach for state estimation in these settings, we present an end-to-end approach for learning state estimators modeled as factor graph-based smoothers. By unrolling the optimizer we use for maximum a posteriori inference in these probabilistic graphical models, this method is able to learn probabilistic system models in the full context of an overall state estimator, while also taking advantage of the distinct accuracy and runtime advantages that smoothers offer over recursive filters. We study our approach using two fundamental state estimation problems, object tracking and visual odometry, where we demonstrate a significant improvement over existing baselines. Our work comes with an extensive code release, which includes the evaluated models and libraries for differentiable Lie theory and factor graph optimization: <https://sites.google.com/view/diffsMOOTHING/>.

I. INTRODUCTION

State estimation is a universal problem in robotics. To make informed decisions, nearly all robots — regardless of whether they are deployed on the ground, in the air, or even in water — must be able to infer the current system state from noisy sensor observations. Traditionally, this problem has been tackled using recursive Bayesian estimators such as Particle or Kalman filters [1], as well as optimization-based smoothing techniques [2]. These algorithms are rooted in probability theory, and require uncertainty-aware models to describe state transitions and how sensor observations relate to system state. The probabilistic underpinnings of these methods have a wide range of practical advantages: information about uncertainty can be used not only for

human interpretability of the inner workings of the state estimator, but also as input to risk-aware planning or control algorithms [3–5].

For many applications, models for these estimators are easy to derive analytically. For pose estimation with inertial measurement units, physically-grounded sensor models can relate angular velocities from a gyroscope, linear accelerations from an accelerometer, and absolute orientations from a magnetometer to information about an egocentric pose. For an inverted pendulum, precise equations of motion can be derived using Newtonian or Lagrangian mechanics. Uncertainty in systems like these can often be effectively approximated as Gaussians with manually-tuned, diagonal covariance matrices.

More complex robotic systems, however, often contain sensors or dynamics that are much harder to pre-specify or tune. This is particularly true for some of the richest, most information-dense sensing modalities, such as images, audio, or tactile feedback, as well as in interaction-rich applications that need to reason about difficult-to-model contact dynamics. These systems also tend to have more complex, heteroscedastic (variable) noise profiles [6]. For example, an object position estimate from an image might rapidly switch from being extremely precise under nominal operating conditions to completely useless under occlusion or poor lighting.

To retain the benefits of a probabilistic state estimator while circumventing the need for analytical models, a recent line of work has shown that we can treat Bayesian filters as a differentiable component of a computation graph [6–10]. These differentiable filters allow end-to-end estimation errors to be backpropagated directly through the structure of the estimator itself, enabling data-driven learning for system models and uncertainties that are optimized for a specific state estimation setting.

In this work, we address this problem of end-to-end learning for probabilistic state estimators modeled as factor

¹ Stanford University {brentyi,michellelee, rober-tom,bohg}@cs.stanford.edu

² Max Planck Institute for Intelligent Systems, akloss@tue.mpg.de

The Toyota Research Institute and Google partially supported this work. This article solely reflects the opinions and conclusions of its authors and not TRI, Google, or any entity associated with TRI or Google.

graph-based smoothers. As detailed in Sec. II-A.3, smoothers have distinct accuracy and runtime advantages over recursive filtering approaches, particularly for more complex or nonlinear applications. Better integrating of smoothing into learning-based systems promises to open these advantages up to a broader set of estimation problems.

The contributions of our work are:

- The introduction of a surrogate loss for end-to-end learning of smoothing-based state estimators, which is computed using a sequence of differentiable optimization steps.
- A study on learning sensor and dynamics models with both constant and heteroscedastic uncertainties, using standard experiments from past differentiable filtering works: 2D visual object tracking and visual odometry.
- A comparison across learnable state estimators and loss functions, which we show outperforms all alternatives on our benchmarks.
- The release of two open-source Python libraries targeted at differentiable optimization, written using JAX [11].

II. BACKGROUND & RELATED WORK

A. State Estimation

In robotics, state estimation has primarily been studied under two frameworks.

1) *Filtering*: Commonly, state estimators are built using a *filtering* structure [1]. In a filter, we maintain a probabilistic belief about the current state of the system, which is most commonly represented as a covariance matrix in Kalman filters or discrete Monte Carlo samples in particle filters. The belief can then be updated at each timestep using incoming sensory inputs. This process requires approximations for non-linear systems, but is recursive in nature and only requires a constant amount of memory for problems with a fixed state dimension: the output at a given timestep t can be computed from only the output from $t-1$ and any inputs corresponding to timestep t .

2) *Smoothing*: In contrast to filtering, smoothing retains all past measurements and continuously recovers full state trajectories. By circumventing the need for an explicit parameterization of the posterior distribution (such as covariance matrices), prior works have shown that smoothers can outperform filtering approaches in terms of both accuracy and runtime [12, 13]. In this work, we study a common graphical approach for representing and solve these problems: factor graphs. Inference on these probabilistic graphical models achieves state-of-the-art results for SLAM problems like visual-inertial odometry [14] and dense 3D mapping [15, 16], but example applications have also included manipulation [17, 18] and optimal control [19].

3) *Why Smoothing?*: While Kalman filters are optimal for simple linear Markov models, abandoning the measurement history in nonlinear systems leads to the permanent buildup of errors from approximations such as model linearization (in Extended Kalman filters) or sigma point belief propagation (in Unscented Kalman filters). As a result, Kalman-type filters risk divergence in applications where these system

approximations are highly state-dependent [17]. In contrast, a factor graph-based smoothing approach gives a user the flexibility to either maintain a full history of inputs or a partial sliding window to balance error reduction with computational efficiency [20]. This results in improved robustness and reduced sensitivity to initialization.

Filtering-based approaches are highly efficient for problems with small state spaces. However, they are limited by the need for an explicit parameterization of the uncertainty of the posterior. For filters with Gaussian assumptions, this is most commonly a covariance or precision matrix. Because these matrices are dense and grow with the square of the state dimensionality, the runtime of filters grows cubically and quickly becomes intractable for systems with large or dynamic state spaces [13]. In contrast, smoothing-based inference can be robustly applied to large-scale systems because computations are inherently sparse, allowing efficient optimization via either sparse matrix factorization [12] or preconditioned conjugate gradient methods [21], and a runtime that grows linearly with state dimensionality [13]. Real-time applications can also benefit from incremental updates to a matrix factorization [20] or Bayes tree data structure [22].

B. Differentiable Filtering

At each time-step, a canonical Bayesian filter updates the posterior belief with a *prediction step* using a dynamics model and a *correction step* using a measurement model. Each of these two steps are generally differentiable, and can be backpropagated through to learn parameters of dynamics and measurement models that directly minimize end-to-end estimation error. This enables data-driven learning of system models and uncertainties that would otherwise be difficult to hand-design or tune.

Haarnoja et al. [7] propose a Kalman filtering-based approach for vision-based state estimation on both a visual tracking task and the KITTI dataset [23]. Similarly, Karkus et al. [8] and Jonschkowski et al. [9] each propose differentiable flavors of the particle filter. Each of these works demonstrate that the structure of a Bayesian filter can be used to improve the performance of a learned state estimator when compared to LSTM-based methods on visual robot localization tasks. In addition to EKFs and Particle filters, Kloss et al. [6] analyses differentiable Unscented Kalman filters and the value of learning heteroscedastic noise models for both KITTI and a planar pushing task. Lee et al. [10] explore differentiable filtering architectures for manipulation tasks involving both vision and touch.

C. Combining Learning & Smoothers

The majority of smoothing approaches assume that analytical models for observations and transitions are available and tractable to evaluate. However, for many state estimation problems, deriving these models may not be obvious and their noise profiles may be difficult to tune. As a result, various works have explored integrating learned components into factor graphs and smoothers. Czarnowski et al. [24]

use depth maps that are predicted by a deep neural network to compute photometric, reprojection, and sparse geometric factors in a Monocular SLAM system. Rabiee and Biswas [25] propose learning a context-dependent noise model to guide feature extraction by avoiding areas that result in noisy correspondences. The correspondences and their estimated noise levels are then used to find the recover camera trajectories. Sodhi et al. [26] proposes the incorporation of tactile measurements into a factor graph to estimate manipulated object poses. Specifically, the authors train an observation model that maps a pair of high-dimensional tactile images to their relative pose with respect to the object frame. The output of this learned function is then integrated along with other factors into the factor graph. [24–26] each learn parameters outside of the smoothing formulation. In contrast, our approach allows learning and fine-tuning models in a completely end-to-end fashion.

Prior work has explored backpropagation through a Kalman-Bucy smoother for learning continuous-time latent dynamics [27] and applied proximal gradient optimization techniques for minimizing prediction errors on Kalman smoothers [28], but end-to-end learning has not been studied for optimization-based smoothers.

D. Differentiable Optimization

Various algorithms have recently been developed for treating optimization itself as a differentiable operation. Notably, Tang and Tan [29] and Jatavallabhula et al. [30] each propose differentiable versions of the Levenberg-Marquardt solver, with the former taking a prediction approach to computing the damping coefficient and the latter choosing a soft reparameterization of the damping coefficient. Similarly, von Stumberg et al. [31] formulate a probabilistic loss based on a single-step Gauss-Newton update. For differentiable optimization through first-order methods, Grefenstette et al. [32] presents tools for unrolling differentiable optimizers in PyTorch.

In the context of factor graphs, Bhardwaj et al. [33] back-propagate through Gauss-Newton updates to learn parameters for Gaussian Process Motion Planning, which formulates trajectory optimization as inference on a factor graph. Our work builds off similar ideas, but is targeted at state estimation.

Notably, Jatavallabhula et al. [30] only demonstrates differentiable optimization for rigid registration between point clouds and Bhardwaj et al. [33] focuses on a specific motion planning algorithm. Both implementations rely on dense matrix computations, with manually specified Jacobians. In contrast, our work uses differentiable optimizers that support arbitrary Gaussian factors and automatically differentiated Jacobians, backed by a sparse matrix computation engine.

III. DIFFERENTIABLE SMOOTHING WITH FACTOR GRAPHS

In this work, we present *differentiable factor graph optimization* for end-to-end optimization of probabilistic smoothers. By interpreting the nonlinear optimization steps used for MAP estimation on a factor graph as a sequence of

differentiable operations, our approach can learn parameters for any state estimator modeled as a factor graph.

A. State Estimation with Factor Graphs

Factor graphs are a class of probabilistic graphical models that have demonstrated impressive versatility in a wealth of real-world robotics problems. By leveraging conditional independence structures, these bipartite graphs represent a probability density over a set of *variables* constrained by *factors*. These factors define conditionally independent density functions on subsets of the variables.

For state estimation problems, we represent the quantities X we want to estimate as variable nodes, and information from system models and sensor observations as factor nodes. Assuming Gaussian noise, each factor encodes a joint probability density for a specific value of X as follows:

$$\phi_i^\theta(X) \propto \exp\left(-\frac{1}{2} \|\mathbf{r}_i^\theta(X)\|_{\Sigma_i^\theta}^2\right) \quad (1)$$

where $\|\cdot\|_{\Sigma_i^\theta}^2$ denotes the squared Mahalanobis norm of an error vector $\mathbf{r}_i^\theta(X)$ under covariance Σ_i^θ . θ contains all factor parameters that can be learned or tuned, which may include physical quantities like masses and inertia matrices, neural network weights, or covariance matrices. In this paper, all terms (values or functions) conditioned on these parameters will be superscripted with θ .

We can now solve for an estimate of the unknown states X – the set of all variables in the factor graph – by performing maximum a posteriori (MAP) inference over the factor graph. Assuming Gaussian noise, this problem reduces to a nonlinear least squares optimization:

$$\begin{aligned} X^{\text{MAP}, \theta} &= \arg \max_X \prod_i \phi_i^\theta(X) \\ &= \arg \max_X \prod_i \exp\left(-\frac{1}{2} \|\mathbf{r}_i^\theta(X)\|_{\Sigma_i^\theta}^2\right) \\ &= \arg \min_X \sum_i \|\Sigma_i^{\theta - \frac{1}{2}} \mathbf{r}_i^\theta(X)\|_2^2 \end{aligned} \quad (2)$$

These types of problems are typically solved using nonlinear optimization approaches such as the Gauss-Newton or Levenberg-Marquardt algorithms, which solve a sequence of linear subproblems around first-order Taylor approximations of the cost function.

B. End-to-end Factor Learning

Traditionally, the factor parameters θ are manually tuned. The key insight that our work builds on is that multi-component systems whose parameters have been optimized end-to-end can perform better than systems whose components are optimized in isolation and brought together [34]. As a substitute for individually tuning each factor in a factor graph, we study end-to-end optimization of the mean-squared error between ground-truth labels X^{gt} and the factor graph's MAP estimate $X^{\text{MAP}, \theta}$:

$$\mathcal{L}_{\text{mse}}(\theta) = \sum_t \|\text{diag}(\boldsymbol{\alpha})(X_t^{\text{gt}} \ominus X_t^{\text{MAP}, \theta})\|_2^2 \quad (3)$$

where t is an index corresponding to each variable in the factor graph and α is a hyperparameter vector that can be used to weight components of the error vectors. \ominus is a generalized subtraction operator, which enables losses for variables on non-Euclidean manifolds like Lie groups.

To enable backpropagation of this loss directly to learnable parameters within the factors, an initial step is to reconstruct MAP inference as a fully differentiable computation graph. Solving for $X^{\text{MAP},\theta}$, however, typically requires running a nonlinear optimizer until a convergence criteria is met. Not only are these problems generally not convex, but the sheer number of iterations that convergence might require means that naively implementing a differentiable nonlinear optimizer and backpropagating the loss in Equation 3 would be computationally prohibitive. For this reason, we propose a surrogate loss $\hat{\mathcal{L}}_{\text{mse}}(\theta)$, which is identical to Equation 3 but replaces supervision on the MAP estimate $X^{\text{MAP},\theta}$ with supervision on a surrogate $\hat{X}^{\text{MAP},\theta}$.

We formulate the computation of $\hat{X}^{\text{MAP},\theta}$ with two properties. First, the surrogate should converge to X^{gt} when the factor parameters have been correctly learned. Second, it must be practical for integration into a mini-batch stochastic gradient descent pipeline.

To fulfill these properties, we propose computing $\hat{X}^{\text{MAP},\theta}$ by (a) initializing a nonlinear optimizer with the ground-truth trajectory and (b) unrolling a constant number of K nonlinear optimization steps, where the last step’s output is supervised in the surrogate loss. During each nonlinear optimization step in a forward pass through steps $k = 0 \dots K - 1$, the computation graph linearizes the MAP cost (from Equation 2) around the current variable values — this outputs a sparse Jacobian — and computes a local update Δ_k^θ by applying a sparse linear solver to the resulting linear subproblem. As an example for $K = 3$, we get:

$$\hat{X}^{\text{MAP},\theta} = ((X^{\text{gt}} \oplus \Delta_0^\theta) \oplus \Delta_1^\theta) \oplus \Delta_2^\theta \quad (4)$$

where \oplus is a generalized addition for supporting manifold retractions.

After applying this sequence of standard nonlinear optimization steps (for example, Gauss-Newton), the surrogate loss can be directly minimized:

$$\hat{\mathcal{L}}_{\text{mse}}(\theta) = \sum_t \|\text{diag}(\alpha)(X_t^{\text{gt}} \ominus \hat{X}_t^{\text{MAP},\theta})\|_2^2 \quad (5)$$

This formulation is desirable for several practical reasons. For example, initializing our optimizer with the ground-truth trajectory sidesteps concerns about convergence: it guarantees that when the target model parameters perfectly match the ground-truth data, $X^{\text{MAP},\theta} = X^{\text{gt}}$, all local update values Δ_k^θ , computed errors, and backpropagated gradients evaluate to zero. Unrolling a fixed number of iterations also has significant advantages for GPU-bound operations. It simplifies batching, eliminates branch and loop overheads, and has a static memory footprint that enables reverse-mode auto-differentiation using tools like Tensorflow XLA.

While we frame this differentiable optimization process as inference on factor graphs, note that the underlying

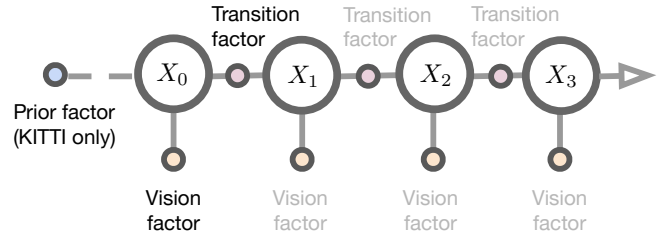


Fig. 2: **Factor graph representation of the smoothers that we learn.** In addition to state variable nodes $X_0 \dots X_{T-1}$, graphs also contain *transition factors* that encode system dynamics, *vision factors* for processing raw images, and for the KITTI visual odometry task *prior factors* that constrain start states.

computations are not tied to this particular probabilistic graphical model. This same approach can be applied to the broad range of similar optimization problems that appear when visualizing these systems as hypergraphs [35], where factor nodes are replaced by hyperedges that can connect any number of variable nodes, and in application-specific algorithms for problems like pose graph optimization [36] and bundle adjustment [13].

IV. EXPERIMENTAL SETUP

A. Visual Tracking

In the first set of experiments, we study a synthetic visual tracking environment that has been used to evaluate differentiable filters [6, 7]. This environment enables full control over the process noise and observation complexity of the underlying system. The goal of this task is to track the motion of a red disk as it moves in 2D space, while occasionally being occluded by distractor discs.

At each timestep t , the state consists of a 2D position \mathbf{p}_t and a 2D velocity \mathbf{v}_t . To generate a dataset for this task, we subject states to discrete-time linear-Gaussian dynamics:

$$\begin{aligned} \mathbf{p}_{t+1} &= \mathbf{p}_t + \mathbf{v}_t + \mathbf{q}_{\mathbf{p},t} \\ \mathbf{v}_{t+1} &= \mathbf{v}_t - f_p \mathbf{p}_t - f_d v_t^2 \text{sign}(v_t) + \mathbf{q}_{\mathbf{v},t} \end{aligned} \quad (6)$$

where \mathbf{q} is Gaussian process noise, f_p is a linear spring coefficient, and f_d is a drag coefficient. For experiments, we use $\mathbf{q}_{\mathbf{v},t} \sim \mathcal{N}(\mathbf{0}, \text{diag}(2, 2))$, $\mathbf{q}_{\mathbf{p},t} \sim \mathcal{N}(\mathbf{0}, \text{diag}(0.1, 0.1))$, $f_p = 0.05$, and $f_d = 0.0075$.

As observations, state estimators have access to $120 \times 120 \times 3$ RGB images. While the position of the red disc can be directly observed when it is visible, the state estimators are faced with the challenge of unobservable velocities, frequent occlusions by 25 other distractor disks in the system, and the fact that the tracked red disk frequently leaves the observable frame. An example observation can be viewed in Figure 4.

We generate 5000 length-20 subsequences for this experiment, split into 10 folds for cross-validation.

To apply the proposed method to learning smoothers for this visual tracking task, we now formalize the factor graph representation depicted in Figure 2.

1) *Transition Factors*: These factors use the analytical dynamics model that we outline in Equation 6 to define joint densities over variable pairs from temporally adjacent timesteps. Given the known process noise covariance \mathbf{Q}_{disk} , forward dynamics model \mathbf{f} , and notation from Equation 1, we define the transition factor as:

$$\mathbf{r}_i(X_t, X_{t+1}) = \mathbf{f}(X_t) - X_{t+1}, \quad \Sigma_i = \mathbf{Q}_{\text{disk}} \quad (7)$$

2) *Learned Vision Factors*: Hand-designing models for processing high-dimensional image inputs is challenging. Therefore, we use a factor with learned parameters for this task. The core component of this factor is a probabilistic virtual sensor model \mathbf{g}^θ , which is shared across all vision factor instantiations. This virtual sensor maps a raw image observation \mathbf{I}_t to a position measurement \mathbf{z}_t^θ and measurement covariance \mathbf{R}_t^θ :

$$(\mathbf{z}_t^\theta, \mathbf{R}_t^\theta) = \mathbf{g}^\theta(\mathbf{I}_t) \quad (8)$$

We can define the resulting factor as:

$$\mathbf{r}_i^\theta(X_t = (\mathbf{p}_t, \mathbf{v}_t)) = \mathbf{z}_t^\theta - \mathbf{p}_t, \quad \Sigma_i^\theta = \mathbf{R}_t^\theta \quad (9)$$

We use the proposed method to learn virtual sensor models with constant \mathbf{R}_t^θ noise profiles, as well as models that output observation-dependent heteroscedastic noise. Implementation details for each case are outlined in Section IV-F.

B. Visual Odometry

To evaluate our approach on real-world data with nonlinear dynamics, we also run experiments on a visual odometry task using the KITTI dataset [23].

The goal of this task is to use image observations for estimating the 5 degree-of-freedom state of a vehicle moving through the world. We represent the variable nodes as $X_t = (\mathbf{T}_t, \mathbf{v}_t, \boldsymbol{\omega}_t)$ where $\mathbf{T} \in \text{SE}(2)$ is a 2D transformation between the world and vehicle body frames, \mathbf{v} is a scalar forward velocity, and $\boldsymbol{\omega}$ is a scalar angular velocity. This is challenging: not only must our state estimator learn to operate using only noisy visual observations, but it also needs to do so in a way that generalizes to novel environments. Our evaluation trajectories are taken exclusively from never-before-seen roads.

To generate data for this task, we reproduce the kitti-10 dataset described in [6]. This consists of 10 distinct trajectories of a car driving down different roads, which we can augment by (a) creating separate samples from each of two available camera feeds and (b) inserting both the original trajectory and a mirrored one into our dataset. We perform 10-fold cross-validation by withholding 1 of these 10 distinct trajectories for testing, and using the remaining 9 for training. Subsequences of length 100 are used for evaluation, but due to the higher computational cost of differentiable smoothing choose training sequences of length 20 instead of 50.

To apply the proposed method to this visual odometry task, we now formalize the factor graph representation depicted in Figure 2.

1) *Transition Factors*: As with many robot odometry tasks, an analytical transition model \mathbf{f} can be accurately hand-specified for the KITTI task. The transition factors take neighboring variable pairs as input and defines two costs: (1) differences between actual and predicted poses at $t+1$ and (2) changes in velocity. By defining the dynamics as a velocity integrator, $\text{SE}(2) \times \mathbb{R}^2 \xrightarrow{\mathbf{f}} \text{SE}(2)$, the transition factor can be written as:

$$\mathbf{r}_i(X_t, X_{t+1}) = \begin{bmatrix} \log(\mathbf{f}(\mathbf{T}_t, \mathbf{v}_t, \boldsymbol{\omega}_t)^{-1} \mathbf{T}_{t+1}) \\ \mathbf{v}_{t+1} - \mathbf{v}_t \\ \boldsymbol{\omega}_{t+1} - \boldsymbol{\omega}_t \end{bmatrix} \quad (10)$$

where $\text{SE}(2) \xrightarrow{\log} \text{se}(2)$ is the logarithmic map on $\text{SE}(2)$.

The dynamics and residual computations have no learnable parameters, but all of the transition factors share a learnable noise covariance $\Sigma_i^\theta = \mathbf{Q}_{\text{KITTI}}^\theta$. We assume the driver's actions to be unknown and they are therefore included in this noise model.

2) *Learned Vision Factors*: Because a vision system on a vehicle must generalize to never-before-seen roads — as is the case in our withheld test trajectory — it is not possible to determine an absolute vehicle pose from visual data. Instead, we follow the formulation established in prior works [6–9] and augment observations for predicting velocities. We stack each raw RGB image channel-wise with a difference frame between the current and previous timesteps. Using this input, we learn a virtual sensor model \mathbf{g}^θ that outputs instantaneous linear and angular velocities:

$$(\mathbf{z}_{\mathbf{v},t}^\theta, \mathbf{z}_{\boldsymbol{\omega},t}^\theta, \mathbf{R}_t^\theta) = \mathbf{g}^\theta(\mathbf{I}_t) \quad (11)$$

Then, the resulting factor can be defined as:

$$\mathbf{r}_i^\theta(X_t = (\mathbf{T}_t, \mathbf{v}_t, \boldsymbol{\omega}_t)) = [\mathbf{z}_{\mathbf{v},t}^\theta - \mathbf{v}_t \quad \mathbf{z}_{\boldsymbol{\omega},t}^\theta - \boldsymbol{\omega}_t]^\top \quad (12)$$

$$\Sigma_i^\theta = \mathbf{R}_t^\theta$$

We again run experiments using virtual sensors with both constant and heteroscedastic noise profiles.

3) *Prior factors*: Because our dynamics and vision factors for this task are only useful for determining relative poses, we additionally introduce an absolute *prior factor*. This factor constrains the estimated trajectory by anchoring the position and velocity of the vehicle at the very first timestep:

$$\mathbf{r}_i(X_0) = \begin{bmatrix} \log((\mathbf{T}_0^{\text{gt}})^{-1} \mathbf{T}_0) \\ \mathbf{v}_0^{\text{gt}} - \mathbf{v}_0 \\ \boldsymbol{\omega}_0^{\text{gt}} - \boldsymbol{\omega}_0 \end{bmatrix} \quad (13)$$

Because this is the only factor that constrains the estimated trajectory's absolute location, the associated covariance can be set to any (numerically stable) positive definite matrix with no impact on converged MAP estimates.

C. Baselines

We present results for three sets of baselines: an alternative probabilistic approach for learning factor parameters, differentiable filters, and general LSTM approaches for state estimation.

1) *Joint NLL Loss*: For learning parameters of the factors, one natural loss function would be to find the parameters that minimize the negative log-likelihood of each ground-truth trajectory X^{label} over the joint distribution specified by the factor graph:

$$\begin{aligned}\mathcal{L}_{\text{nll}}(\theta) &= -\log \prod_i \phi_i^\theta(X^{\text{gt}}) \\ &= -\sum_i \log(\phi_i^\theta(X^{\text{gt}})) \\ &= -\sum_i \left(\log \|\mathbf{r}_i^\theta(X^{\text{gt}})\|_{\Sigma_i^\theta}^2 + \log |\Sigma_i^\theta| \right)\end{aligned}\quad (14)$$

where constant terms have been omitted. In contrast to the proposed end-to-end surrogate loss, note that the Joint NLL Loss baseline is equivalent to learning the parameters of each factor in isolation.

2) *Differentiable Filter Baselines*: As baselines for alternative probabilistic state estimators that are optimized end-to-end, we use differentiable recursive filters, as studied in [6–10]. In contrast to the global optimization performed by a smoother, recursive filters operate by running a single forward pass over the observation sequence.

For the visual tracking task described in Section IV-A, we evaluate on a differentiable Kalman filter with Equation 6 as the dynamics model. The measurement \mathbf{z}_t and covariance \mathbf{R}_t are computed using the virtual sensor model \mathbf{g}_θ in Equation 9.

For the visual odometry task described in Section IV-B, we utilize Equation 10 as dynamics model and \mathbf{z}_t and \mathbf{R}_t are computed using the virtual sensor model \mathbf{g}_θ in Equation 12. After receiving \mathbf{z}_t from the virtual sensor, the measurement model for each estimation task reduces to a linear selection matrix. Differentiable filter baselines for the visual odometry task use the same implementations from [6], but are retrained. We include *Extended Kalman Filter* (dEKF), *Particle Filter with Gaussian Mixture Model* (dPF-M), and *Unscented Kalman Filter* (dUKF).

3) *LSTM Baselines*: Following prior work on differentiable filtering [6–10], we also compare to a long-short-term memory (LSTM) [37] baseline. We implement unidirectional LSTM baselines as in past work, as well as a bidirectional LSTM [38], which, similar to a smoothing framework, conditions each state estimate on both prior and subsequent observations. For both the visual odometry and tracking task, the LSTM and bidirectional LSTMs directly regress estimated states. For the visual odometry task, we additionally include the LSTM model implemented and trained in [6], which includes a dynamics model that uses the LSTM-learned velocities to calculate the position and orientation of the car. We call this baseline *LSTM + Dynamics*.

D. Evaluation Metrics

For evaluation on the visual tracking task, we follow prior work [6, 7] and evaluate the *root mean square error* (RMSE) between the entire estimated and ground truth trajectory.

For the visual odometry task, we follow prior work [6–9] and only compare the final timestep in the estimated

(1) 3x conv(3x3, 32, relu), conv(3x3, 32)
(2) Channel-wise max pool
(3) Concatenate width-mean pool and height-mean pool
(4) fc(32, relu)
(5) fc(2)

fc: fully connected, conv: convolution

TABLE I: **Virtual sensor architecture for regressing visual tracking.**
Outputs are X/Y position estimates.

trajectory against ground truth. In this task, the estimate will drift over time. Therefore, the final estimate is a good proxy to evaluate the estimation quality over the entire trajectory. In addition, this final estimate is conditioned on all measurements in all approaches (filters, smoothers, uni- and bidirectional LSTMs). We report two terms: (i) *Translational* (m/m), the positional error at the last time step normalized by ground-truth distance traveled, and (ii) *Rotational* (deg/m), angular error at the last time step normalized by ground-truth distance traveled.

E. Loss Functions

Smoothers are trained using either the end-to-end surrogate loss or a joint NLL loss (Equation 14), while filters match [6] and are trained on either an end-to-end MSE (visual tracking, visual odometry) or end-to-end marginal NLL (visual tracking) losses. For the KITTI visual odometry smoothers, we report separate results for end-to-end supervision on position MSE (X and Y, weighted equally) and velocity MSE (linear and angular, in normalized units). LSTM baselines supervise the full state vector, in normalized units.

F. Implementation Details

1) *Nonlinear Optimizers*: We implement nonlinear optimization steps using Gauss-Newton updates with $K = 10$ for computing surrogate losses, and Levenberg-Marquardt for evaluating trained models. Linear subproblems are solved with the Jacobi-preconditioned conjugate gradient method. Note that optimizer convergence is trivial for the visual tracking task, as all factor residuals are linear.

2) *Network Architectures*: The virtual sensor architecture for visual tracking can be found in Table I. For virtual sensors that output heteroscedastic noise, we have a separate network that inputs the # of visible red pixels to a 4x fc(64, relu) and fc(1), which outputs the inverse standard deviation (following [6]).

The implementation of the LSTMs for the visual tracking task follows the same architecture as the virtual sensors, but expands the hidden unit count of the final dense layer to 32. The output is then passed to an LSTM cell with a hidden state size 64, followed by another 32-unit dense layer, ReLU, then 2-unit dense layer. A bidirectional LSTM is the same architecture as the LSTM, but two times the hidden state size.

For the KITTI visual odometry task, we follow the same network architectures as [6]. While the LSTM baseline by Kloss et al. [6] outputs linear and angular velocities and is used in conjunction with a dynamics model to calculate the

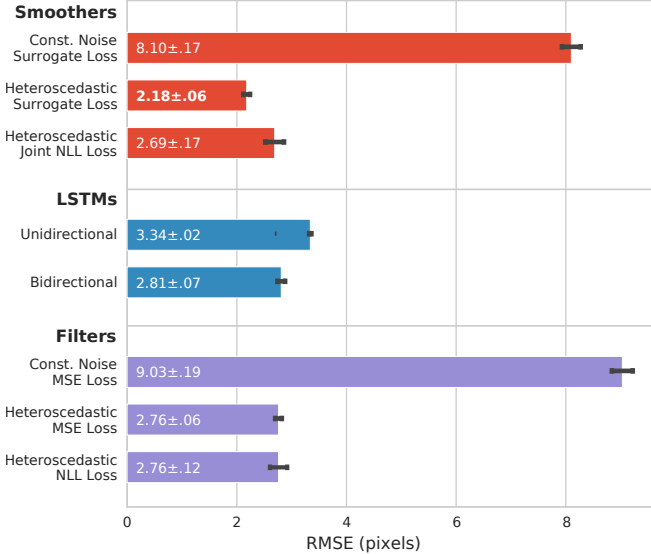


Fig. 3: **Test set errors on the visual tracking task.** We report mean and standard error metrics for smoothers, LSTMs, and Kalman filters across each of the 10 folds. A smoother trained using the end-to-end surrogate loss outperforms all baselines.

Model Type		m/m	deg/m
Smoothers	Surrogate Loss, Vel	.235 ± .018	.1880 ± .0389
	Surrogate Loss, Pos	.112 ± .033	.0300 ± .0065
	Joint NLL Loss	.615 ± .101	.0537 ± .0086
Smoothers	Surrogate Loss, Vel	.214 ± .042	.0618 ± .0191
	Surrogate Loss, Pos	.131 ± .014	.0475 ± .0092
	Joint NLL Loss	.203 ± .027	.0489 ± .0075
	Hand-tuned Noise	.183 ± .029	.0419 ± .0096
LSTMs	Unidirectional	1.168 ± .139	.588 ± .0994
	Bidirectional	1.393 ± .395	.532 ± .0914
	LSTM + Dynamics	.538 ± .057	.0788 ± .0083
Differentiable Filters [6]	dEKF	.211 ± .034	.0766 ± .0069
	dUKF	.180 ± .023	.0799 ± .0083
	dPF-M	.206 ± .018	.0764 ± .0072

TABLE II: **Evaluation results on the KITTI visual odometry task.** As with the visual tracking task, an end-to-end optimized smoother with a heteroscedastic noise model outperforms all alternatives.

position and orientation of the car, we follow Jonschkowski et al. [9] by additionally comparing to LSTMs that have been modified to directly regress car positions and (the cosine and sine of) absolute orientations.

V. EXPERIMENTAL EVALUATION

A. Overview

By integrating the structure of a probabilistic smoother with end-to-end optimization, our approach aims to provide performance benefits over (i) purely learned models such as LSTMs, which contain less task-specific structure, (ii) state estimators with models that are trained outside of the overall estimator, which do not explicitly supervise end-to-end estimation error, and (iii) differentiable filtering approaches, which suffer from limitations intrinsic to recursive filtering. We test this hypothesis by evaluating the proposed approach and baselines on the tasks detailed in Section IV.

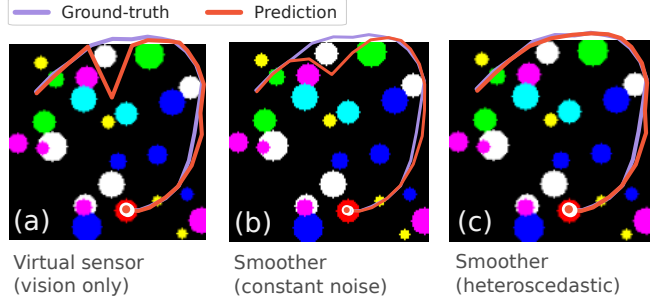


Fig. 4: **Visual tracking trajectories overlayed on a first-timestep observation.** We plot (a) predictions from the virtual sensor of a learned vision factor, (b) a smoothing output after learning constant virtual sensor uncertainties, and (c) a smoothing output after learning heteroscedastic uncertainties. A smoother with a heteroscedastic noise model is able to correctly reason about erroneous visual measurements when the disk exits the frame.

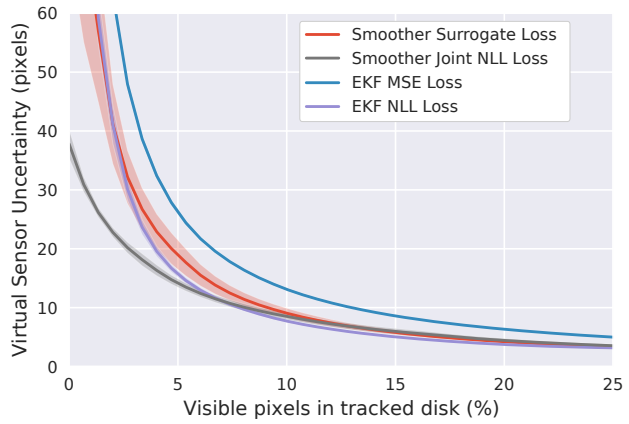


Fig. 5: **Outputs of heteroscedastic noise models learned for the visual tracking task.** After training, the three end-to-end losses (Smusher Surrogate, EKF MSE, and EKF NLL) converge to high uncertainties when the disk is occluded; these indicate the absence of information that can be used for state estimation. In contrast, the Joint NLL Loss simply learns the RMSE of the prediction error.

B. Overall Estimation Accuracy

The results for the visual tracking task can be found in Figure 3, and the results for the visual odometry task are in Table II. We find that the end-to-end optimized differentiable smoothers outperform baselines on both tasks. These results support our overall hypothesis that our approach performs better than less structured LSTMs, and that the algorithmic advantages seen in traditional smoothers carry into learned settings.

Notably, we also see in both tasks that heteroscedastic noise models are essential for performance. While assuming constant noise parameters is common and often required for the feasibility of hand-tuned uncertainties, relying on them significantly drops tracking performance.

C. Analyzing uncertainties

As with standard, hand-tuned probabilistic state estimators, end-to-end-optimized smoothers enable the direct inspection of uncertainties. Not only can this be useful for

	Tested on Filter	Tested on Smoother
Trained on Filter	$2.758 \pm .056$	$2.332 \pm .128$
Trained on Smoother	$2.803 \pm .062$	$2.175 \pm .060$

TABLE III: **Heteroscedastic noise model transfer results.** Visual tracking noise models learned using the end-to-end surrogate loss for smoothers are evaluated in a filter, and noise models learned using end-to-end (MSE) optimization of a filter are evaluated in a smoother. We observe a significant performance increase when the training context matches the evaluation context.

	Noise 0.0	Noise 0.1	Noise 0.3
$K = 1$	0.172 ± 0.027	0.216 ± 0.030	0.218 ± 0.031
$K = 3$	0.136 ± 0.023	0.153 ± 0.023	0.212 ± 0.029
$K = 10$	0.131 ± 0.014	0.139 ± 0.015	0.153 ± 0.018

TABLE IV: **Surrogate loss ablation results.** We vary optimizer step counts (K) and initialization noise levels for computing the end-to-end surrogate losses. All quantities are positional tracking errors (m/m) on the KITTI task.

downstream decision-making, but analyzing these uncertainties can also reveal why certain state estimators outperform others. Figure 5 visualizes learned heteroscedastic noise models for virtual sensors trained on the visual tracking task. Compared to using the Joint NLL Loss baseline, in which factors are trained in isolation, approaches that are trained end-to-end assign higher uncertainties to measurements when the disk is occluded. This highlights the key role that end-to-end training plays for performance. When factors are trained in isolation using the Joint NLL Loss baseline, virtual sensor uncertainties converge to the prediction RMSE. The associated uncertainty, therefore, is bound by the size of the area that the disk traverses. This is optimal only when the errors are truly zero-mean Gaussians, which is rarely true in practice. In contrast, end-to-end methods are able to correctly reason that, when placed in context of the overall state estimator, vision factors provide no contribution when the tracked disk is fully occluded.

D. Transferring noise models

A key motivation for our approach is the possibility of learning system models that are specifically optimized for the smoothing task that they are deployed in. Filters and smoothers make a different set of assumptions: it can thus be concluded that a model that is optimized for filtering is not necessarily the same as a model that is optimized for smoothing. To quantify this, we evaluate the transfer of heteroscedastic noise profiles between state estimation frameworks for the visual tracking task. Noise profiles are optimized in a filter and evaluated in a smoother, and vice versa. Results are shown in Table III.

Compared to an end-to-end learned smoother, we observe a significant drop in performance when using a filter-trained model within a factor graph-based smoother. We see a similar drop when implanting smoother-trained noise models into a filter. These results underline the simple insight that drives the utility of our method: in order to make the most out of available training data, it is important for model parameters to be learned in the same context that they are evaluated in.

E. Surrogate Loss Ablation

To build insight on the end-to-end surrogate loss, we study the effect of varying K , the optimizer step count, as well as the ground-truth initialization of the nonlinear optimizer. We train constant noise smoothers on the visual odometry task with K set to 1, 3, and 10. For evaluating the impact of the ground-truth initialization, we inject Gaussian noises with standard deviations of 0.0, 0.1, and 0.3 into the normalized (standard deviation scaled to 1.0) state vectors used to initialize the nonlinear optimizer. Results for combinations of these parameters are presented in Table IV.

Adjusting the number of unrolled steps of K can be seen as interpolating between supervising a linear approximation of the factor graph ($K = 1$) and the exact MAP estimate of the nonlinear factor graph ($K = \infty$, assuming convergence). The results are consistent with this intuition: we see a decrease in estimation errors as we increase K and supervise better MAP estimate approximations. The difference in position estimate error between $K = 3$ and $K = 10$, however, is low, suggesting diminishing returns as we increase the number of times we optimize through the smoother. In future work, we can explore gradually increasing K during training, so that the factor graph first uses quick and rough gradient computations, before iteratively refining the parameters to produce better approximations of the MAP estimate.

We hypothesized originally that initializing the nonlinear optimizer to the ground-truth trajectory was beneficial for shaping the convergence properties for the MAP surrogate $\hat{X}^{\text{MAP}, \theta}$. The ablation results are consistent with this motivation as well: the performance of the model gradually drops as the optimizer is initialized with trajectories further and further away from the ground-truth.

VI. CONCLUSION

In this work, we propose an approach for probabilistic state estimation that integrates optimization-based smoothing into a end-to-end optimized system. By backpropagating gradients through a fixed number of nonlinear optimization steps, our method can be used to learn smoothers that outperform both LSTMs and differentiable filters, while retaining the many advantages of probabilistic state estimation.

Given the widespread adoption of both factor graph optimization and end-to-end learning in robotics, we are excited about the practical implications of these results and the directions for future work that they open up. Immediate applications exist where standard factor-graph based methods have outperformed filtering, which includes state estimation in the context of SLAM, robot locomotion, and manipulation. We plan to explore applying this method to additional sensing modalities, such as audio or tactile feedback, where factor graphs have in part been constrained by the difficulty of analytical factor design. Finally, we plan to investigate how our method can be integrated into a broader range of end-to-end optimized robot learning systems, particularly ones that enable tighter coupling of perception and control.

REFERENCES

[1] S. Thrun, W. Burgard, and D. Fox, *Probabilistic Robotics (Intelligent Robotics and Autonomous Agents)*. The MIT Press, 2005.

[2] F. Dellaert and M. Kaess, *Factor Graphs for Robot Perception*, 2017.

[3] W. Li and E. Todorov, “Iterative linearization methods for approximately optimal control and estimation of non-linear stochastic system,” *International Journal of Control*, vol. 80, no. 9, pp. 1439–1453, 2007.

[4] B. Pontón, S. Schaal, and L. Righetti, *On the Effects of Measurement Uncertainty in Optimal Control of Contact Interactions*. Cham: Springer International Publishing, 2020, pp. 784–799.

[5] C. Eppner, R. Martín-Martín, and O. Brock, “Physics-based selection of informative actions for interactive perception,” in *2018 IEEE International Conference on Robotics and Automation (ICRA)*. IEEE, 2018, pp. 7427–7432.

[6] A. Kloss, G. Martius, and J. Bohg, “How to train your differentiable filter,” *Autonomous Robot*, 2020, submitted.

[7] T. Haarnoja, A. Ajay, S. Levine, and P. Abbeel, “Backprop kf: Learning discriminative deterministic state estimators,” in *Advances in Neural Information Processing Systems*, 2016, pp. 4376–4384.

[8] P. Karkus, D. Hsu, and W. S. Lee, “Particle filter networks with application to visual localization,” in *Conference on Robot Learning*, 2018, pp. 169–178.

[9] R. Jonschkowski, D. Rastogi, and O. Brock, “Differentiable Particle Filters: End-to-End Learning with Algorithmic Priors,” in *Proceedings of Robotics: Science and Systems (RSS)*, 2018.

[10] M. A. Lee, B. Yi, R. Martín-Martín, S. Savarese, and J. Bohg, “Multimodal sensor fusion with differentiable filters,” in *2020 IEEE/RSJ International Conference on Intelligent Robots and Systems (IROS)*, 2020, pp. 10444–10451.

[11] J. Bradbury, R. Frostig, P. Hawkins, M. J. Johnson, C. Leary, D. Maclaurin, G. Necula, A. Paszke, J. VanderPlas, S. Wanderman-Milne, and Q. Zhang, “JAX: composable transformations of Python+NumPy programs,” 2018. [Online]. Available: <http://github.com/google/jax>

[12] F. Dellaert and M. Kaess, “Square root sam: Simultaneous localization and mapping via square root information smoothing,” *The International Journal of Robotics Research*, vol. 25, no. 12, pp. 1181–1203, 2006.

[13] H. Strasdat, J. M. Montiel, and A. J. Davison, “Visual slam: why filter?” *Image and Vision Computing*, vol. 30, no. 2, pp. 65–77, 2012.

[14] S. Leutenegger, S. Lynen, M. Bosse, R. Siegwart, and P. Furgale, “Keyframe-based visual–inertial odometry using nonlinear optimization,” *Int. J. Rob. Res.*, vol. 34, no. 3, p. 314–334, Mar. 2015. [Online]. Available: <https://doi.org/10.1177/0278364914554813>

[15] R. F. Salas-Moreno, R. A. Newcombe, H. Strasdat, P. H. J. Kelly, and A. J. Davison, “Slam++: Simultaneous localisation and mapping at the level of objects,” in *2013 IEEE Conference on Computer Vision and Pattern Recognition*, 2013, pp. 1352–1359.

[16] T. Whelan, M. Kaess, H. Johannsson, M. Fallon, J. J. Leonard, and J. McDonald, “Real-time large-scale dense rgb-d slam with volumetric fusion,” *The International Journal of Robotics Research*, vol. 34, no. 4-5, pp. 598–626, 2015.

[17] K.-T. Yu and A. Rodriguez, “Realtime state estimation with tactile and visual sensing for inserting a suction-held object,” in *2018 IEEE/RSJ International Conference on Intelligent Robots and Systems (IROS)*, 2018, pp. 1628–1635.

[18] A. S. Lambert, M. Mukadam, B. Sundaralingam, N. D. Ratliff, B. Boots, and D. Fox, “Joint inference of kinematic and force trajectories with visuo-tactile sensing,” in *International Conference on Robotics and Automation, ICRA 2019, Montreal, QC, Canada, May 20-24, 2019*. IEEE, 2019, pp. 3165–3171.

[19] D.-N. Ta, M. Kobilarov, and F. Dellaert, “A factor graph approach to estimation and model predictive control on unmanned aerial vehicles,” in *2014 International Conference on Unmanned Aircraft Systems (ICUAS)*. IEEE, 2014, pp. 181–188.

[20] V. Indelman, S. Williams, M. Kaess, and F. Dellaert, “Factor graph based incremental smoothing in inertial navigation systems,” in *2012 15th International Conference on Information Fusion*. IEEE, 2012, pp. 2154–2161.

[21] Y.-D. Jian, D. C. Balcan, and F. Dellaert, “Generalized subgraph preconditioners for large-scale bundle adjustment,” in *Outdoor and Large-Scale Real-World Scene Analysis*. Springer, 2012, pp. 131–150.

[22] M. Kaess, H. Johannsson, R. Roberts, V. Ila, J. J. Leonard, and F. Dellaert, “isam2: Incremental smoothing and mapping using the bayes tree,” *The International Journal of Robotics Research*, vol. 31, no. 2, pp. 216–235, 2012.

[23] A. Geiger, P. Lenz, C. Stiller, and R. Urtasun, “Vision meets robotics: The kitti dataset,” *The International Journal of Robotics Research*, vol. 32, no. 11, pp. 1231–1237, 2013.

[24] J. Czarnowski, T. Laidlow, R. Clark, and A. Davison, “Deepfactors: Real-time probabilistic dense monocular slam,” *IEEE Robotics and Automation Letters*, vol. 5, pp. 721–728, 2020.

[25] S. Rabiee and J. Biswas, “Iv-slam: Introspective vision for simultaneous localization and mapping,” in *Conference on Robot Learning*, 2020.

[26] P. Sodhi, M. Kaess, M. Mukadam, and S. Anderson, “Learning tactile models for factor graph-based state estimation,” in *2021 IEEE International Conference on Robotics and Automation*, 2021, submitted.

[27] A. Li, P. Wu, and M. Kennedy, “Replay Overshooting: Learning stochastic latent dynamics with the extended kalman filter,” in *2021 International Conference on Robotics and Automation (ICRA)*, 2021.

[28] S. T. Barratt and S. P. Boyd, “Fitting a kalman smoother to data,” in *2020 American Control Conference (ACC)*, 2020, pp. 1526–1531.

[29] C. Tang and P. Tan, “BA-net: Dense bundle adjustment networks,” in *International Conference on Learning Representations*, 2019.

[30] K. M. Jatavallabhula, G. Iyer, and L. Paull, “ ∇ slam: Dense slam meets automatic differentiation,” in *2020 IEEE International Conference on Robotics and Automation (ICRA)*, 2020, pp. 2130–2137.

[31] L. von Stumberg, P. Wenzel, Q. Khan, and D. Cremers, “GN-Net: The gauss-newton loss for multi-weather relocalization,” *IEEE Robotics and Automation Letters (RA-L)*, vol. 5, no. 2, pp. 890–897, 2020.

[32] E. Grefenstette, B. Amos, D. Yarats, P. M. Hüt, A. Molchanov, F. Meier, D. Kiela, K. Cho, and S. Chintala, “Generalized inner loop meta-learning,” *arXiv preprint arXiv:1910.01727*, 2019.

[33] M. Bhardwaj, B. Boots, and M. Mukadam, “Differentiable gaussian process motion planning,” in *2020 IEEE International Conference on Robotics and Automation (ICRA)*, 2020, pp. 10598–10604.

[34] P. Karkus, X. Ma, D. Hsu, L. P. Kaelbling, W. S. Lee, and T. Lozano-Pérez, “Differentiable algorithm networks for composable robot learning,” in *Robotics: Science and Systems XV, University of Freiburg, Freiburg im Breisgau, Germany, June 22-26, 2019*, A. Bicchi, H. Kress-Gazit, and S. Hutchinson, Eds., 2019.

[35] R. Kümmerle, G. Grisetti, H. Strasdat, K. Konolige, and W. Burgard, “G2o: A general framework for graph optimization,” in *2011 IEEE International Conference on Robotics and Automation*, 2011, pp. 3607–3613.

[36] E. Olson, J. Leonard, and S. Teller, “Fast iterative alignment of pose graphs with poor initial estimates,” in *Proceedings 2006 IEEE International Conference on Robotics and Automation*, 2006. ICRA 2006., 2006, pp. 2262–2269.

[37] S. Hochreiter and J. Schmidhuber, “Long short-term memory,” *Neural Computation*, vol. 9, no. 8, pp. 1735–1780, 1997.

[38] M. Schuster and K. K. Paliwal, “Bidirectional recurrent neural networks,” *IEEE transactions on Signal Processing*, vol. 45, no. 11, pp. 2673–2681, 1997.